A Universal Deposition Protocol for Planar Heterojunction Solar Cells with High Efficiency Based on Hybrid Lead Halide Perovskite Families. — Source link ↗

Bert Conings, Bert Conings, Aslihan Babayigit, Aslihan Babayigit ...+9 more authors

Institutions: University of Hasselt, University of Oxford, Linköping University, University of Antwerp

Topics: Solar cell, Thin film and Perovskite (structure)

Related papers:

- Cesium-containing triple cation perovskite solar cells: improved stability, reproducibility and high efficiency

- Solvent engineering for high-performance inorganic–organic hybrid perovskite solar cells

- Organometal Halide Perovskites as Visible-Light Sensitizers for Photovoltaic Cells

- Incorporation of rubidium cations into perovskite solar cells improves photovoltaic performance

- High-performance photovoltaic perovskite layers fabricated through intramolecular exchange

A universal deposition protocol for planar heterojunction solar cells with high efficiency based on hybrid lead halide perovskite families

A universal deposition protocol for planar heterojunction solar cells with high efficiency based on hybrid lead halide perovskite families

Bert Conings,*[a,b] Aslihan Babayigit[§,a,b] Matthew T. Klug[§,b] Sai Bai,[b, c] Nicolas Gauquelin,[d] Nobuya Sakai,[b] Jacob Tse-Wei Wang,[b] Johan Verbeeck,[d] Hans-Gerd Boyen,[a] Henry J. Snaith*[b]

[a] Hasselt University, Institute for Materials Research, Wetenschapspark 1, 3590 Diepenbeek, Belgium. E-mail: bert.conings@uhasselt.be

[b] Clarendon Laboratory, Department of Physics, University of Oxford, Oxford OX1 3PU, United Kingdom. Email: henry.snaith@physics.ox.ac.uk

[c] Biomolecular and Organic Electronics, IFM, Linköping University, Linköping 58183, Sweden.

[d] Electron Microscopy for Materials Research (EMAT), University of Antwerp, Groenenborgerlaan 171, 2020 Antwerp, Belgium.

* bert.conings@uhasselt.be; Henry.Snaith@physics.ox.ac.uk

[§] A.B. and M.T.K. contributed equally to this work

Since the first demonstrations of solid-state photovoltaic (PV) devices based on organic-inorganic halide perovskite absorbers, these materials have attracted tremendous attention and intrigued many researchers by their ability to effortlessly surpass the efficiency of competing state-of-the-art technologies right from their introduction.[1-4] After a mere few years of successive leaps in fundamental understanding and experimental insight, perovskites have become a front runner of the photovoltaic research scene, and represent the fastest developing solar technology in history. The current record power energy conversion efficiency (PCE) is at 22.1%, on par with CdTe and closely approaching the champion efficiency of silicon, the industry flagship material.[5] As a consequence, the prospect of their large-scale application has become virtually undeniable, even though several key challenges must be addressed including mitigating the environmental impact of Pb- and Sn-based perovskites,[6, 7] proving long term operational stability, and producing reliable and efficient manufacturing techniques for large-area deposition. Beyond PV, the beneficial optical and charge transport properties of perovskites have enabled their successful deployment in other optoelectronic applications, including light emitting diodes, photodiodes and lasers, which further highlight their potential to disruptively impact these markets.[8-10]

As the field of perovskite optoelectronics developed, a plethora of strategies has arisen to control their electronic and morphological characteristics for the purpose of producing high efficiency devices. A number of deposition methods have been proposed, the most prominent ones including one step coating,[1, 2] several varieties of sequential deposition,[11, 12] anti-solvent quenching,[13] vapour assisted deposition,[14] thermal evaporation,[15] vacuum assisted solvent drying,[16] and variations on these.[17] On the other hand, much efforts have been invested in altering the precursor composition to induce better film quality, for example by using different solvents,[11, 18, 19] the addition of acid(s)[20-22] or other additives,[23, 24] or the use of sacrificial components that assist in film formation during a subsequent annealing step.[2, 25, 26] Unfortunately, despite the wealth of deposition approaches, the community experiences a great deal of irreproducibility between different laboratories and preparation methods.[27] Another remarkable point is that the viability of most –if not all– of the aforementioned film

enhancement strategies through deposition and precursor engineering have been established by demonstrating the successful operation of one particular perovskite composition and device architecture. Exchanging anions or cations in the perovskite matrix, or switching the device configuration, typically produces inferior results with the same parameter window, and a rigorous optimization cycle is required each time to eventually realize the full potential of a particular newly developed perovskite composition in or device design.[28] This has prompted the investigation of many creative (post-)treatments to enhance the film morphology, again specific to a certain type of perovskite. For instance, halide exchange has been employed to transfer the beneficial morphology of one type of perovskite to a variety of halide compositions.[29, 30] Also the possibility has been shown to dissolve and recrystallize a rough methylammonium lead triiode (MAPbI$_3$) film by exposure to methylamine gas, and a cation exchange with formamidinium (FA) can be made in an extension of this method using formamidine gas.[31, 32] Even hot pressing, a method inherited from metallurgy, has been explored for film smoothening.[33] While the effectiveness of these and related techniques is convincing, they are indirect routes and significant effort is required to adapt them for the fabrication of new perovskite compositions. Likewise, perovskite formation appears to often be sensitive to small changes in local conditions, which has contributed to widespread issues of irreproducibility between laboratories. Thus, it has become apparent that there is a pressing need for a universal and uncomplicated deposition strategy that is applicable for many compositions of perovskite and is insensitive to minor changes in deposition conditions. Aiming to address this issue, we present in this Communication a simple deposition method based on gas quenching that yields smooth films for very different perovskite compositions, ranging from the widely investigated MAPbI$_3$ to triple cation perovskites, and produces planar heterojunction devices with competitive efficiencies.

Huang et al. reported a gas quenching method for the first time, where a gas flow is directed towards the sample during spin coating of a dimethylformamide (DMF)-based precursor, resulting in a smooth layer of MAPbI$_3$ and corresponding average efficiencies of around 16%.[34] Despite this early demonstration, an extension has only recently been made to FAPbI$_3$, but therein the addition of hydroiodic acid was essential for achieving efficiencies above 3%.[35] Gas quenching has also been reported as an additional crystallization accelerator together with anti-solvent quenching to produce ultra-smooth MAPbI$_3$ films, but no improvement in efficiency was observed in comparison.[36] We show here that this still relatively unexplored method of gas quenching can in fact be exploited as a general
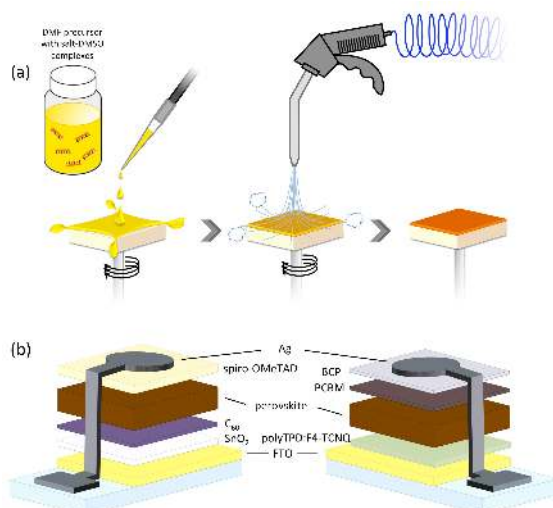

Fig. 1: (a) Schematic of the different steps of the complex-assisted gas quenching technique; (b) device architecture for the n-i-p devices (left) and p-i-n devices (right).

tool to produce smooth pinhole-free perovskite films regardless of composition, based on spin coating (and is likely transferable to upscalable techniques)[37], with no need for sacrificial components, antisolvents or additional post-treatments (that is, apart from the usual annealing step). As will be demonstrated, the key to the generality of the technique is the addition of dimethylsulfoxide (DMSO) to a DMF-based precursor solution. This is based on the rationale that complexes form between the former and the precursor salts, which subsequently develop into intermediate crystalline entities upon evaporation of the parent solvent DMF, thereby retarding the otherwise fast reaction between the ingredients.[13, 38-46] The exploitation of this DMSO-PbX$_2$ complexation phenomenon has been introduced in the context of solvent quenching, where the intermediate phase is obtained by "freezing" the precursor compounds upon quenching a wet film with an antisolvent to quickly wash off the parent solvent.[13] We show here that the removal of the parent solvent is achieved equally effectively and more robustly by using gas quenching, rather than liquid rinsing. **Fig. 1a** shows a simple schematic of this technique. After a few seconds into the spin coating process, the timing of which depends on spin speed and precursor concentration, a stream of nitrogen is directed towards the still wet film. This drastically expedites the evaporation of the parent solvent and thereby creates a two-fold crystallization-retarding effect which (i) induces the formation of complexes, and (ii) drives the system to a state of supersaturation at a rate quicker than the kinetics of heterogeneous nucleation, thereby preventing the growth of irregular or dendritic structures that would otherwise result in an uneven film containing many holes.[47] The procedure then ends with the freshly quenched substrate being placed on a hot plate and annealed as usual. To demonstrate the generality of this complex-assisted gas quenching (CAGQ) method, we applied it to deposit a selection of both well-studied and state-of-the-art perovskites as reported in recent literature.[13, 20, 48-50] This comprises perovskites with different single, double or triple A-site cations (methylammonium (MA), formamidinium (FA), Cs), and single or double X-site anions (I, Br), with corresponding varied band gaps. Obviously, many different stoichiometries are available within such a selection of single and composite cation perovskites, and we have chosen the ones deemed most relevant to the community.

Fig. 2 shows an overview of top-view Scanning Electron Microscopy (SEM) images of the films with different perovskite composition, formed on a fluorine-doped SnO$_2$ (FTO)/SnO$_2$/C$_{60}$ substrate to mimic the conditions for the corresponding solar cells, as will be discussed later. First of all, to validate the relevance of gas quenching, the morphology of layers of MAPbI$_3$, FA$_{0.85}$MA$_{0.15}$Pb(I$_{0.9}$Br$_{0.1}$)$_3$, FA$_{0.85}$Cs$_{0.15}$Pb(I$_{0.95}$Br$_{0.05}$)$_3$, and (FA$_{0.83}$MA$_{0.17}$)$_{0.95}$Cs$_{0.05}$Pb(I$_{0.9}$Br$_{0.1}$)$_3$ made without (Fig. 2a-d) and with quenching (Fig. 2e-f) is shown. The first figures are divided in a low and a high magnification panel for an adequate representation of both the larger features and their substructure. It can be easily noticed that there is a dramatic difference in morphology between the two cases. Without gas quenching, uneven structures more commonly arise, with either acicular shaped crystallites (Fig. 2a1) or interconnected bowl-like shapes (Fig. 2b1-c1-d1). The magnitude of this effect is slightly damped by the presence of DMSO, but there is still a conspicuous signature of quick heterogeneous nucleation.[47, 51] The surface coverage is still acceptable for MAPbI$_3$ (Fig. 2a1), with only a few pinholes, whereas the mixed perovskites show micron-sized craters. This is also reflected in the corresponding optical absorption spectra of these films (see **Fig. S1**). Comparing now with gas quenched layers made from the same precursors, it is immediately obvious that these are smoother and completely pinhole-free. The morphology is very comparable to what is reported for solvent quenched films, as is the grain size of a

few hundred nanometers.[13] Corresponding X-ray Diffraction (XRD) data can be found in **Fig. S2** and reveal that, in the case of mixed cations, more unreacted PbI_2 is present for gas-quenched films. The reason for this difference is unclear, but its presence is expected from the excess PbI_2 which we purposefully added in all the precursor solution. [52]

Interestingly, large crystallites on the order of 2μm are observed for a pure $FAPbI_3$ film while maintaining the smoothness and the absence of pinholes (Fig. 2i). Given that the fabrication of $FAPbI_3$ films of decent morphological quality has been proven challenging,[20, 53] our observation truly underlines the robustness of CAGQ. Also higher band gap perovskites, with higher Cs and Br content, benefit from CAGQ. We fabricated $FA_{0.8}Cs_{0.2}Pb(I_{0.65}Br_{0.35})_3$ and $FA_{0.75}Cs_{0.25}Pb(I_{0.70}Br_{0.30})_3$ perovskites with band gaps of 1.73 eV and 1.76 eV, respectively, as recently suggested for tandem applications[48] and, inspired by those, $(FA_{0.83}MA_{0.17})_{0.80}Cs_{0.20}Pb(I_{0.65}Br_{0.35})_3$, a triple cation perovskite of 1.77 eV that has not been previously reported, in Fig. 2j, k and l, respectively. In all cases, a very similar morphology is found as for the lower band gap perovskites, with only a difference in grain size.

All of these perovskite layers have been implemented in solar cell stacks as depicted in Fig. 1b, first in an n-i-p configuration, that uses SnO_2 passivated with C_{60} as the electron conductor, and spiro-OMeTAD as hole transporter material. To further demonstrate the universal viability of CAGQ, inverted devices for three different perovskites compositions were fabricated using poly[N,N'-bis(4-butylphenyl)-N,N'-bis(phenyl)benzidine] (polyTPD) doped with 2,3,5,6-Tetrafluoro-7,7,8,8-tetracyanoquinodimethane (F4-TCNQ) as the hole transporter and [6,6]-phenyl-C61-butyric acid methyl ester (PCBM) as the electron transporter. Table 1 provides a complete overview of the corresponding photovoltaic characterization.‡ Non-quenched layers in devices 2-4 deliver unsatisfactory performance in all aspects, which one would expected based on their incomplete coverage (Fig. 2b-d). It is noteworthy that the unquenched $MAPbI_3$ (device 1) in fact exhibits only a minor concentration of pinholes, but delivers an equally substandard performance. This suggests that the charge recombination at the interface between the hole and electron transporters is not the root cause of the poor performance for the unquenched layers. Instead, we propose the lack of intimate contact between the perovskite and its scaffold is a more likely culprit.
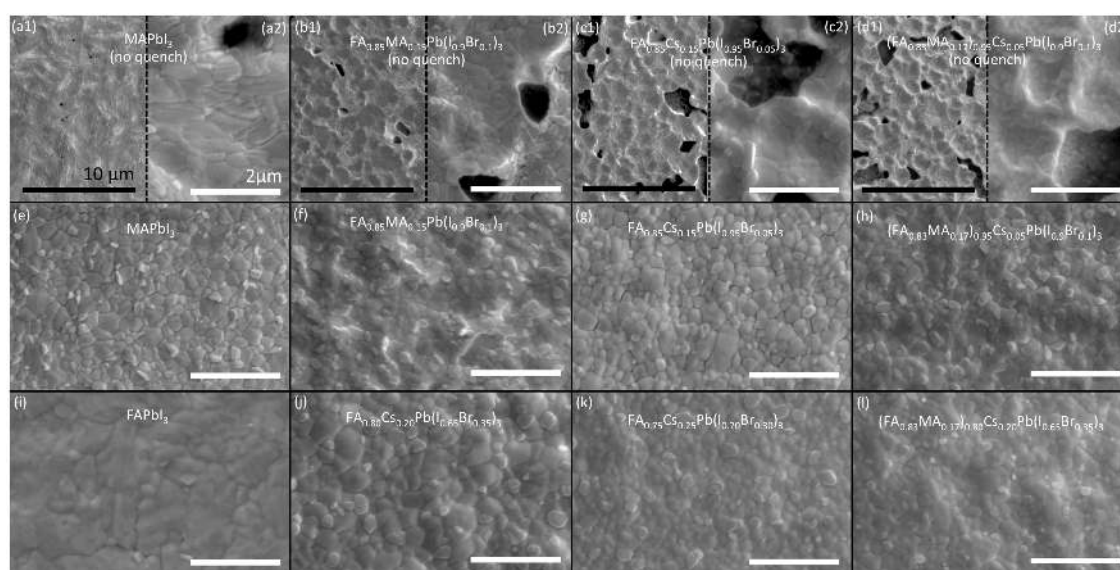

Fig. 2: SEM images of a selection of perovskite layers fabricated on from DMF precursors with added DMSO for complex formation. (a)-(d): as spun; (e)-(l): gas quenched. Black scale bars: 10μm, white scale bars: 2μm.

In comparison, the corresponding solar cells with gas-quenched layers perform much better. Very decent efficiencies were obtained, where the stabilized power output (SPO) was close to or even higher than the backward current density-voltage (JV) scan. An SPO of up to 17.7% was achieved for MAPbI$_3$ (device 5), which is among the higher end of reported values for this material. In comparison, we show that devices made in the absence of DMSO (device 6) exhibit a larger spread in results and a markedly decreased fill factor (corresponding with the presence of pinholes, as seen in Fig. S4), which clearly proves the effectiveness of complexes in the precursor. Also for neat FAPbI$_3$ (device 7), and the increasingly popular composite-cation FA/MA and FA/Cs families (devices 8 and 9), competitive efficiencies between 15 and 17% were obtained. An average efficiency of 18% and a maximum of 18.9% were even achieved for a triple cation perovskite (device 10), which is the first report of high efficiency planar cells of this type after the seminal paper by Saliba *et al.* using the mesoporous TiO$_2$ architecture, and confirms their observations in terms of efficiency regarding the addition of 5% Cs in a FA/MA cation mixture.[49] **Fig. 3a** shows the forward and reverse JV characteristics of the best triple cation device, where a noticeable degree of hysteresis is present. Although the unfortunate pervasiveness of hysteresis in perovskite solar cells is often found to have a negative influence on the SPO, we observe SPOs close to, or sometimes even higher than the efficiency from reverse JV scans, resulting in a maximum obtained SPO of 18.5% in this case (see Fig. 3b). The gravity of the presence of hysteresis in our devices is further moderated by the current consensus that the presence of hysteresis itself would not be detrimental for long-term stability.[54] A cross-sectional SEM image of the champion device is depicted in Fig. 3c, confirming the high quality perovskite layer with crystallites that extend vertically in the order of the layer thickness.

Also our large band gap CAGQ deposited perovskites (around 1.75 eV) perform very well. The average SPO values of these mixed cation devices (device 11-13) are on par with the recent work by McMeekin et al., at about 12%.[48] For completeness, we also demonstrate the possibility of triple cation cells with higher Cs and Br content to deliver a larger band gap (device 13). Unfortunately they perform slightly less than their large band gap double cation counterparts (devices 11 and 12), especially in terms of SPO, which fits within the observation by Saliba et al. that excessive Cs content negatively impacts the performance of an otherwise FA/MA based perovskite.[49]

It also should be mentioned that the time window for the start of the gas quenching is quite flexible, as illustrated in **Fig. S10**, which again bodes well for the robustness of the technique.

material	quench (Y/N)	measured band gap [V]	device configuration	J_{sc} [mA·cm^{-2}]	V_{oc} [V]	FF [-]	PCE [%]	SPO [%]
1. MAPbI$_3$	N	1.58	n-i-p	16.3±1.2 17.7	0.81±0.07 0.86	0.53±0.11 0.55	7.5±0.7 8.5	4.3±2.9 6.3
2. FA$_{0.85}$MA$_{0.15}$Pb(I$_{0.9}$Br$_{0.1}$)$_3$	N	1.55	n-i-p	17.0±1.3 18.2	0.81±0.09 0.88	0.50±0.06 0.56	6.3±2.2 8.0	5.7±1.8 6.9
3. FA$_{0.85}$Cs$_{0.15}$Pb(I$_{0.95}$Br$_{0.05}$)$_3$	N	1.55	n-i-p	18.4±1.8 20.3	0.90±0.03 0.92	0.46±0.05 0.54	7.7±2.3 10.0	8.4±2.0 9.8
4. (FA$_{0.83}$MA$_{0.17}$)$_{0.95}$Cs$_{0.05}$Pb(I$_{0.9}$Br$_{0.1}$)$_3$	N	1.55	n-i-p	18.3±1.0 19.5	0.91±0.09 0.92	0.58±0.04 0.68	8.9±0.6 9.61	9.6±0.2 9.8
5. MAPbI$_3$	Y	1.61	n-i-p	21.2±0.7 22.1	1.05±0.02 1.08	0.74±0.02 0.76	16.5±0.4 17.0	16.7±0.6 17.7
6. MAPbI$_3$ (from pure DMF)	Y	1.59	n-i-p	21.4±1.2 23.0	1.01±0.02 1.08	0.66±0.04 0.72	14.6±1.3 16.6	13.9±1.6 15.3
7. FAPbI$_3$	Y	1.52	n-i-p	22.3±0.3 22.5	0.96±0.02 0.98	0.75±0.01 0.76	16.1±0.4 16.5	16.0±0.3 16.2
8. FA$_{0.85}$MA$_{0.15}$Pb(I$_{0.9}$Br$_{0.1}$)$_3$	Y	1.57	n-i-p	21.9±0.5 22.9	1.07±0.01 1.10	0.72±0.02 0.74	16.6±0.5 17.1	16.8±0.5 17.6
9. FA$_{0.85}$Cs$_{0.15}$Pb(I$_{0.95}$Br$_{0.05}$)$_3$	Y	1.59	n-i-p	21.5±0.7 22.4	0.98±0.02 1	0.70±0.02 0.74	14.7±1.0 16.1	14.8±0.3 15.0
10. (FA$_{0.83}$MA$_{0.17}$)$_{0.95}$Cs$_{0.05}$Pb(I$_{0.9}$Br$_{0.1}$)$_3$	Y	1.58	n-i-p	22.6±0.5 23.4	1.08±0.03 1.12	0.74±0.02 0.77	18.0±0.5 18.9	18.0±0.6 18.5
11. FA$_{0.8}$Cs$_{0.2}$Pb(I$_{0.65}$Br$_{0.35}$)$_3$	Y	1.76	n-i-p	16.9±0.4 17.2	1.08±0.01 1.1	0.70±0.02 0.73	12.5±0.7 13.6	12.2±0.2 12.4
12. FA$_{0.75}$Cs$_{0.25}$Pb(I$_{0.70}$Br$_{0.30}$)$_3$	Y	1.73	n-i-p	17.1±0.4 17.7	1.06±0.01 1.08	0.67±0.03 0.71	12.2±0.7 13.5	11.0±0.5 11.7
13. (FA$_{0.83}$MA$_{0.17}$)$_{0.80}$Cs$_{0.20}$Pb(I$_{0.65}$Br$_{0.35}$)$_3$	Y	1.77	n-i-p	16.5±0.8 17.1	1.07±0.01 1.08	0.69±0.02 0.72	12.0±0.6 12.6	10.3±0.3 10.8
14. MAPbI$_3$	N	1.58	p-i-n	13.5±2.0 16.2	0.81±0.07 0.96	0.60±0.01 0.62	6.6±0.7 7.7	5.5±1.1 3.7
15. (FA$_{0.83}$MA$_{0.17}$)$_{0.95}$Cs$_{0.05}$Pb(I$_{0.9}$Br$_{0.1}$)$_3$	N	1.55	p-i-n	11.2±2.6 14.1	0.10±0.11 0.35	0.19±0.10 0.29	0.3±0.5 1.4	0.7±0.7 1.2
16. FA$_{0.8}$Cs$_{0.2}$Pb(I$_{0.65}$Br$_{0.35}$)$_3$	N	1.76	p-i-n	14.1±0.5 14.6	0.91±0.06 1.02	0.49±0.05 0.58	6.3±1.2 8.7	4.9±0.9 6.2
17. MAPbI$_3$	Y	1.61	p-i-n	18.9±0.9 20.6	1.04±0.01 1.04	0.79±0.01 0.80	15.6±0.8 16.6	16.1±0.2 16.6
18. (FA$_{0.83}$MA$_{0.17}$)$_{0.95}$Cs$_{0.05}$Pb(I$_{0.9}$Br$_{0.1}$)$_3$	Y	1.58	p-i-n	20.0±1.0 21.0	0.95±0.03 0.99	0.78±0.03 0.82	15.4±1.1 16.9	15.6±0.6 16.5
19. FA$_{0.8}$Cs$_{0.2}$Pb(I$_{0.65}$Br$_{0.35}$)$_3$	Y	1.76	p-i-n	14.3±0.6 15.1	1.07±0.01 1.08	0.76±0.02 0.79	11.6±0.5 12.3	11.6±0.4 12.1

Table 1: List of perovskites fabricated in this work, their band gap as determined from steady state photoluminescence measurements (see **Fig. S3**), and their photovoltaic performance in n-i-p or p-i-n device configuration. J_{sc}, V_{oc}, FF and PCE values are averages with standard deviations, extracted from backward JV-scans of at least 16 devices (4 devices for SPO). The value at the bottom of each cell in the table is the maximum obtained value. SPO curves of the best devices can be found in **Fig. S6-S9**.
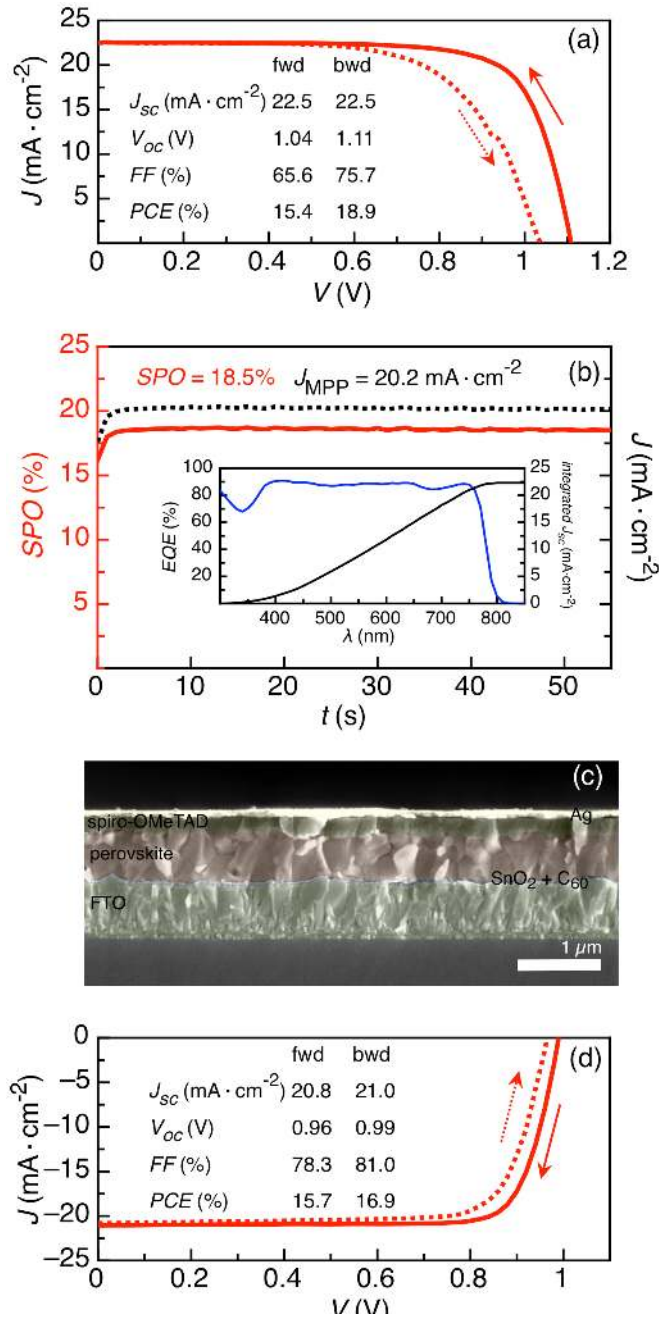
Fig. 3: Forward and backward JV characteristics (a), SPO curve (b) (inset: EQE spectrum), and a cross-sectional colour-enhanced SEM image (c) of the champion $(FA_{0.83}MA_{0.17})_{0.95}Cs_{0.05}Pb(I_{0.9}Br_{0.1})_3$ solar cell in planar n-i-p configuration. (d) JV characteristics of the best $(FA_{0.83}MA_{0.17})_{0.95}Cs_{0.05}Pb(I_{0.9}Br_{0.1})_3$ cell in p-i-n configuration.

A great deal of the progress made in perovskite research is based on the inverted device architecture (p-i-n).[55] We now further emphasize the universality of CAGQ deposition by applying it to fabricate $MAPbI_3$ and triple cation $(FA_{0.83}MA_{0.17})_{0.95}Cs_{0.05}Pb(I_{0.9}Br_{0.1})_3$, and large band gap $FA_{0.8}Cs_{0.2}Pb(I_{0.65}Br_{0.35})_3$ layers in inverted device stacks of the form FTO/polyTPD/perovskite/PCBM/BCP/Ag (devices 14-19). Non-quenched layers perform even more inadequately in p-i-n configuration (devices 14-16), whereas using CAGQ (devices 17-19, JV characteristics to be found in Fig. S11), efficiencies of +16% are obtained for $MAPbI_3$ and the triple cation perovskite, and competitive values of around 12% for the 1.76 eV $FA_{0.8}Cs_{0.2}Pb(I_{0.65}Br_{0.35})_3$ perovskite, all comparable to their n-i-p versions and thereby clearly substantiating the viability of the CAGQ in a broader context.

With this we are also the first to report an inverted triple cation perovskite solar cell. Fig. 3d shows the forward and reverse JV characteristics of the best $(FA_{0.83}MA_{0.17})_{0.95}Cs_{0.05}Pb(I_{0.9}Br_{0.1})_3$ device. In contrast with the n-i-p case, in the p-i-n configuration the triple cation variant is (despite its higher J_{sc}) overall not more efficient than $MAPbI_3$, mainly due to an average deficiency of 90 mV in V_{oc} compared to the latter, so this does leave room for improvement. The underlying reason could be related to interface energetics, but resolving this issue is beyond the scope of the current work. Generally, the obtained photocurrents of our p-i-n devices are somewhat lower than for their n-i-p counterparts, yet we are confident this is not related to the deposition method as this is a general observation in p-i-n devices that can be attributed to charge carrier recombination at the interface of the perovskite and sub-optimal hole acceptor layers.[56, 57] Finally, we find very high fill factors of up to over 80%, among the highest reported for the inverted architecture.[55]

In a recent work, different composition-dependent morphologies were reported for a wide compositional space of $FA_xMA_{1-x}Pb(I_yBr_{1-y})_3$ perovskites, also using DMF-based precursors containing DMSO/salt complexes (as in the current work), but deposited by the anti-solvent quenching method.[28] It was found that the morphological appearance was not always a valid proxy for device performance. While this extensive work delivers valuable information on the shifting physical mechanisms as a function of perovskite composition, it also clearly supports our claim that CAGQ is a more widely applicable deposition method, as it consistently delivers high efficiencies for different perovskite varieties, within and outside the $FA_xMA_{1-x}Pb(I_yBr_{1-y})_3$ family.

We now turn our attention to a high-angle annular dark field scanning transmission electron microscopy (HAADF-STEM) study to examine the quality of CAGQ deposited films and their interaction with adjacent layers more thoroughly. To this end, a cross-sectional sample of a complete $MAPbI_3$ solar cell was prepared using the focused ion beam (FIB) method (as described in a previous work[58]), shown in **Fig. 4a**. The perovskite crystalline domains of a few hundred nanometers in size are easily recognizable and corroborate the result from SEM in Fig. 2e. At higher magnification (Fig. 4b), lattice fringes are observed, delineating crystalline areas of sizes down to 5-10 nm, much smaller than the domains themselves. Thin dashed red lines are added in Fig. 4b as a guide to the eye, clearly indicating lattice planes with different orientation, and suggesting a polycrystalline character. **Fig. S12** shows additional images where also larger crystalline areas are observed, up to more than 50 nm. Together with an estimated grain size of about 100 nm obtained from Debye-Scherrer analysis of the corresponding diffractogram in Fig. S2, it is safe to conclude that the perovskite film consists of a mixture of both larger and smaller grains, but definitely smaller than the domain size as seen from SEM (Fig. 2e). A selected area diffraction (SAED) pattern from a 400 nm grain (see Fig. 4c) indeed further confirms that it comprises different crystallites (more ring-like diffraction pattern). This contradicts some prior reports where perovskite crystallites in high efficiency devices were found to be actual single crystals (sharp diffraction pattern).[34, 59] Interestingly, the fact that our perovskite layers –thus compromised in this aspect– still deliver efficiencies on par with or higher than those earlier reports could suggest that single crystalline properties are not a fundamental requirement for highly performing perovskite solar cells. This is particularly intriguing in the light of very recent findings of metallic rather than semiconducting behaviour of perovskite single crystals under illumination at room temperature.[60]

We identify the 2-5 nm white structures in the perovskite, clearly observed in Fig. 4d, as PbI_2, based on our previous experience with STEM measurements on this material.[58] From this prior work, we rule out

An interesting observation is the discernible discontinuity of the C_{60} layer: discrete lumps are sitting on the SnO_2 instead of forming an actual film. This is even clearer in Fig. 4d where a higher magnification of the SnO_2/C_{60} layers is shown. Electron Energy Loss Spectroscopy (EELS) mapping (Fig. 4e) was performed to rule out any suspicion of these darker structures just being voids, and thereby an indication of local film delamination. From the Sn $M_{4,5}$, O K, and In $M_{4,5}$ edge maps, it can be seen that the position of the ITO and SnO_2 layers is pinpointed very precisely and the flat character of the SnO_2 is confirmed. Considering the C signal, is it obvious that a more carbonaceous but discontinuous region is present at the interface between the perovskite and the SnO_2. This is conclusive evidence that C_{60} is partially redissolved upon the deposition of the perovskite from (mainly) DMF, as proposed before.[61, 62] Notably, where these earlier reports suggested the unattainability of decent device performance due to this effect, our devices are still highly efficient despite the defective fullerene layer. This discrepancy in observations can however be explained. First of all, revisiting Fig. 4d in more detail, the SnO_2 layer appears nanoporous rather than compact. Secondly, upon closer inspection of the C signal in Fig. 4e, it can be noticed that there is a very faint enrichment of carbon in the region that corresponds to the SnO_2. These findings imply that the fullerene has infiltrated into the SnO_2 matrix (as aggregates and/or just as a physisorbed monolayer), and thus prevents the SnO_2 from being directly contacted by the perovskite. As a monolayer of fullerene suffices to passivate the metal oxide, it is more than conceivable that such SnO_2/C_{60} composite can adequately fulfil the same function of a planar stacked SnO_2/C_{60}.[63, 64]
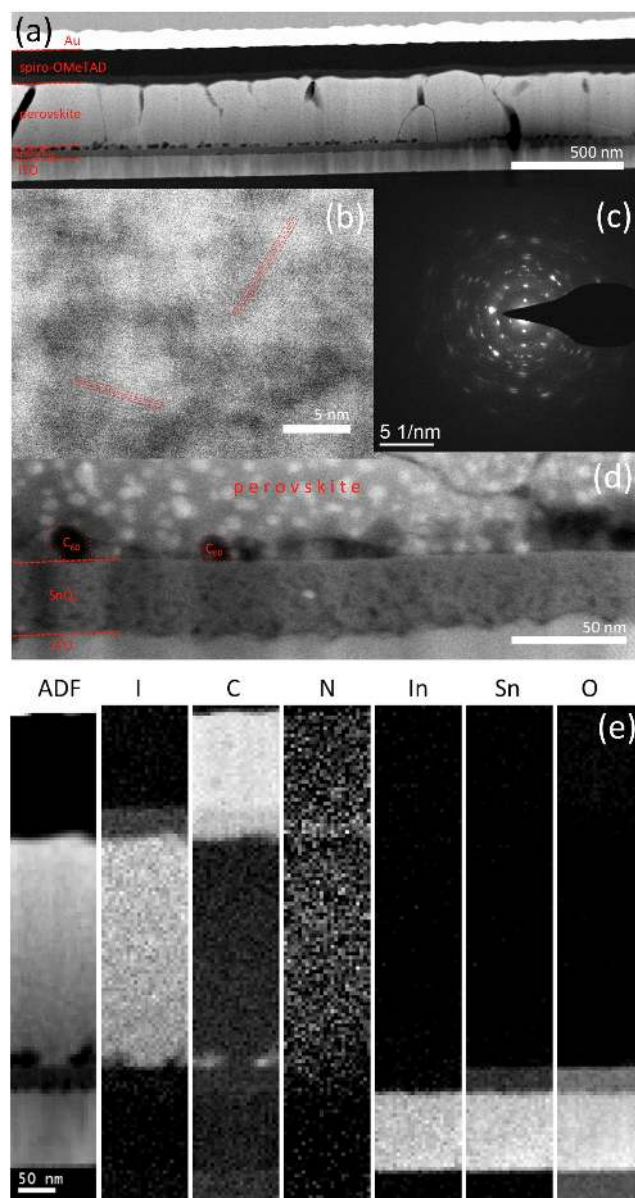
Fig. 4: (a) HAADF-STEM cross sectional image of a CAGQ deposited MAPbI$_3$ solar cell. A Au top contact is used here to facilitate the FIB preparation. (b) High resolution detail of the center of a perovskite grain where lattice plains can be observed. (c) SAED diffraction pattern of a large grain of the perovskite film, showing its polycrystalline character. (d) Detail of the ITO/SnO$_2$/C$_{60}$/perovskite interface regions. (e) EELS mapping of the complete layer stack using the I M$_{4,5}$, C K, N K, In M$_{4,5}$, Sn M$_{4,5}$ and O K edges, together with the corresponding simultaneously acquired ADF signal.

Conclusions

In this work, we have reported a DMSO-PbX$_2$ complex assisted gas quenching (CAGQ) solution deposition method, to fabricate pinhole-free perovskite layers. It is demonstrated that the method is generally applicable for many different compositional varieties relevant for solar cells. The perovskite crystallites in highly performing solar cells were found to be polycrystalline, though it is still under investigation whether this is necessarily a handicap towards performance. The proposed method represents a considerable step towards better reproducibility among laboratories by offering a reliable strategy for the deposition of numerous existing perovskites and can serve as a convenient tool for the screening of

novel perovskite compositions as well. Considering its simplicity and robustness, it can undoubtedly be implemented in large-area coating procedures such as blade coating, and therefore offers a compelling advantage in the road towards scaling up the solution processed perovskite photovoltaic technology.

Experimental

Preparation of solutions

0.2M $SnCl_2$ (Alfa Aesar) was dissolved in ethanol. 10mg/ml C_{60} was dissolved in 1,2-dichlorobenzene and stirred overnight. Perovskite precursor solutions were prepared by dissolving the desired combinations of MAI (Dyesol), FAI (Dyesol), PbI_2 (Sigma), $PbBr_2$ (Sigma) and CsI (Alfa Aesar) in typical concentrations of 1 - 1.35 M in DMF. For use in the n-i-p structure, 2.5% excess PbI_2/$PbBr_2$ was added. An amount of DMSO was then added, in slight excess of stoichiometric equality with the Pb ions, which is equivalent to an approximate 9:1 DMF:DMSO ratio for a 1.35M precursor. The solutions were sonicated for 15 minutes, and filtered before use. Spiro-OMeTAD was dissolved in chlorobenzene (72.3mg/ml) with the addition of 28.8µl 4-butylpyridine and 17.5µl of a 520mg/ml stock solution of Li-TFSI in acetonitrile.

Fabrication of n-i-p solar cells

FTO glass (TEC7, Hartford) was patterned with zinc powder and 2M HCl solution, and subsequently ultrasonically cleaned with Hellmanex soap solution, water, acetone and 2-propanol. Right before the deposition of the $SnCl_2$ solution, the samples were treated with oxygen plasma for 5 minutes. The $SnCl_2$ films were then heated at 185°C in air for at least one hour to form SnO_2. C_{60} was spin coated on the SnO_2 at 3500rpm. The samples were then transferred to a nitrogen-filled glovebox. The perovskite precursor was spin coated and a strong nitrogen flow was directed towards the sample from a distance of a few inches, after a certain time, depending on the concentration and spin speed. Typically, a spin speed of 3000 rpm was used for a 1.35M precursor, and the N_2 stream was applied 10 seconds into the spin coating process. The N_2 stream was sustained between 5 to 8 seconds. Equivalently, for a number of precursor compositions, a colour change from very pale yellow to orange or brown can be observed upon quenching, and the N_2 stream can be terminated once the colour change has happened. The method allows for a comfortable deposition window (see Fig. S10). Films made with increased DMSO content required postponed quenching times but yielded the same efficiency. The pressure on the nitrogen line was about 6 bar, but equally high quality films could be obtained at slightly lower pressures by restricting the flow. The samples were then heated for 30 minutes at 150°C (for pure FA and FA-Cs based films) or 60 minutes at 100°C (all others, except only 10 minutes for $MAPbI_3$). Spiro-OMeTAD was spin coated on top at 3000 rpm, after which the samples were stored in a desiccator overnight. Finally, a Ag top contact (~100nm) was evaporated under high vacuum (~6×10^{-6} Torr).

Fabrication of p-i-n solar cells

Patterning and cleaning of FTO was carried out in the same manner described in the previous section but with TEC15 FTO (Hartford). The TEC15 FTO substrates were further cleaned with piranha solution at room temperature for at least 90 minutes, followed by rinsing in water, DI water, ethanol, and drying with N_2. The hole transport layer was prepared on the piranha-treated FTO by spin coating a hot solution (110°C) containing 1 mg/mL poly-TPD (1-Material) and 0.2 mg/mL F4-TCNQ (Sigma) in toluene at 2krpm

for 30s, followed by annealing in ambient at 110°C for 10 minutes.[65] Once cooled to room temperature, the substrates were transferred into a nitrogen atmosphere for spin coating the remaining layers. Perovskite solutions were prepared and deposited in a similar manner to the n-i-p devices.

MAPbI$_3$ was spun from a 1.0 M solution at 4000 rpm, (FA$_{0.83}$MA$_{0.17}$)$_{0.95}$Cs$_{0.05}$Pb(I$_{0.9}$Br$_{0.1}$)$_3$ was spun from a 1.2 M solution at 5000 rpm, and (FA$_{0.80}$Cs$_{0.20}$)Pb(I$_{0.65}$Br$_{0.35}$)$_3$ was spun from a 1.1 M solution at 4000 rpm. The N$_2$ stream was applied at 12 seconds into the process and sustained for 8 seconds. Afterwards, the perovskite films were immediately placed on a hot plate and annealed as for the n-i-p cells. PCBM (20 mg/mL in chlorobenzene) was spin coated at 1.8krpm for 30s, followed by a short annealing at 100°C for 10 minutes prior to the deposition of BCP (0.5 mg/mL in IPA) at 4krpm for 20s. The devices were finished by the evaporation of a Ag contact (100nm)

Characterization

Current density-voltage (JV) characteristics were recorded in ambient environment by a Keithley 2400 source meter under AM1.5G simulated sunlight at 100 mW cm^{-2} (Abet Class AAB Sun 2000 Simulator), with calibrated intensity by means of an NREL calibrated KG5-filtered Si reference cell (mismatch factor <1%). The solar cells were masked with a black metal mask, exposing a device area of 0.092cm^2. JV scans were measured by scanning from forward bias to short circuit (backward scan) and from short circuit to forward bias (forward scan) at a rate of 0.38 V/s. The stabilized power output was measured by measuring the current while holding the voltage at the maximum power point from the backward scan. EQE was measured on a home-built setup fitted with a Newport 6257 xenon lamp (100 W), a Newport Cornerstone 130 monochromator (with sorting filters) and a Stanford Research Systems SR830 lock-in amplifier. The light beam was mechanically chopped at 21 Hz. Calibration was done with an FDS-100 calibrated silicon photodiode. A Hitachi S-4300 field emission scanning electron microscope was used for morphological characterization. Steady-state PL measurements were carried out with a Fluo Time 300 Fluorescence Lifetime Spectrometer (PicoQuant FmbH). Perovskite films were excited using a 507 nm laser pulsed at frequencies between 1 MHz and 10 MHz. X-ray diffraction spectra were obtained from perovskite films on FTO/SnO$_2$/C60, using a Panalytical X'Pert Pro X-ray diffractometer. Absorption spectra were measured on a Varian Cary 300 UV-Vis spectrometer.

For the preparation of FIB lamellae, solar cells were first transferred inside the glove box into a Kammrath&Weiss Gmbh transfer module together with the Focused Ion Beam (FIB) copper support grid and then transferred to the FIB (FEI Helios 650). In this case, we used ITO as transparent electrode because of its lower roughness compared to FTO, in order to minimize interface blurring in the EELS analysis as a consequence of the finite FIB lamella thickness. We are confident this is representative as the device performance on ITO and FTO are identical. After the FIB lamella was prepared, the transfer module was then opened again inside the glove box and the FIB sample was transferred into a Gatan double-tilt vacuum transfer holder for TEM investigation. The vacuum transfer holder was then inserted inside a FEI Titan 60-300 microscope equipped with an X-FEG high brightness electron source, a probe Cs corrector, a Super-X 4-quadrant EDX detector and a Gatan GIF Enfinium electron energy loss (EEL) spectrometer. The microscope was operated at 120 kV in Scanning TEM mode with a low electron dose to avoid electron-induced damage to the perovskite. Imaging was performed with a 21 mrad convergence angle and collection of all electrons in the range 46–160 mrad for high angle annular dark

field (HAADF). EDX and monochromated core-loss and low-loss EELS measurements were performed with a beam current of ≈50 pA.

Acknowledgements

Notes and references

‡ Devices made from different compositions are referred to as "device x" from now on, even though the results for each composition is based on a statistic of a set of identically prepared devices.

[1]   H.-S. Kim, C.-R. Lee, J.-H. Im, K.-B. Lee, T. Moehl, A. Marchioro, S.-J. Moon, R. Humphry-Baker, J.-H. Yum, J. E. Moser, M. Graetzel, N.-G. Park, *Sci. Rep.* **2012**, *2*, 591.
[2]   M. M. Lee, J. Teuscher, T. Miyasaka, T. N. Murakami, H. J. Snaith, *Science* **2012**, *338*, 643.
[3]   W. Zhang, G. E. Eperon, H. J. Snaith, *Nature Energy* **2016**, *1*, 16048.
[4]   C. Zuo, H. J. Bolink, H. Han, J. Huang, D. Cahen, L. Ding, *Adv. Sci.* **2016**, DOI: 10.1002/advs.201500324.
[5]   http://www.nrel.gov/ncpv/images/efficiency_chart.jpg, Vol. accessed 9th June 2016.
[6]   A. Babayigit, D. Duy Thanh, A. Ethirajan, J. Manca, M. Muller, H.-G. Boyen, B. Conings, *Sci. Rep.* **2016**, *6*, 18721.
[7]   A. Babayigit, A. Ethirajan, M. Muller, B. Conings, *Nat. Mater.* **2016**, *15*, 247.
[8]   L. Dou, Y. Yang, J. You, Z. Hong, W.-H. Chang, G. Li, Y. Yang, *Nat. Commun.* **2014**, *5*, 5404.
[9]   H. Zhu, Y. Fu, F. Meng, X. Wu, Z. Gong, Q. Ding, M. V. Gustafsson, M. T. Trinh, S. Jin, X. Y. Zhu, *Nat. Mater.* **2015**, *14*, 636.
[10]   F. Li, C. Ma, H. Wang, W. Hu, W. Yu, A. D. Sheikh, T. Wu, *Nat. Commun.* **2015**, *6*, 8238.
[11]   J. Burschka, N. Pellet, S.-J. Moon, R. Humphry-Baker, P. Gao, M. K. Nazeeruddin, M. Graetzel, *Nature* **2013**, *499*, 316.
[12]   Z. Xiao, C. Bi, Y. Shao, Q. Dong, Q. Wang, Y. Yuan, C. Wang, Y. Gao, J. Huang, *Energy Environ. Sci.* **2014**, *7*, 2619.
[13]   N. J. Jeon, J. H. Noh, Y. C. Kim, W. S. Yang, S. Ryu, S. Il Seol, *Nat. Mater.* **2014**, *13*, 897.
[14]   Q. Chen, H. Zhou, Z. Hong, S. Luo, H.-S. Duan, H.-H. Wang, Y. Liu, G. Li, Y. Yang, *J. Am. Chem. Soc.* **2014**, *136*, 622.
[15]   M. Liu, M. B. Johnston, H. J. Snaith, *Nature* **2013**, *501*, 395.
[16]   X. Li, D. Bi, C. Yi, J.-D. Décoppet, J. Luo, S. M. Zakeeruddin, A. Hagfeldt, M. Grätzel, *Science* **2016**, *DOI: 10.1126/science.aaf8060*, DOI: 10.1126/science.aaf8060.
[17]   A. Sharenko, M. F. Toney, *J. Am. Chem. Soc.* **2016**, *138*, 463.
[18]   B. Conings, L. Baeten, C. De Dobbelaere, J. D'Haen, J. Manca, H.-G. Boyen, *Adv. Mater.* **2014**, *26*, 2041.
[19]   M. Lv, X. Dong, X. Fang, B. Lin, S. Zhang, J. Ding, N. Yuan, *RSC Adv.* **2015**, *5*, 20521.
[20]   G. E. Eperon, S. D. Stranks, C. Menelaou, M. B. Johnston, L. M. Herz, H. J. Snaith, *Energy Environ. Sci.* **2014**, *7*, 982.
[21]   W. Zhang, S. Pathak, N. Sakai, T. Stergiopoulos, P. K. Nayak, N. K. Noel, A. A. Haghighirad, V. M. Burlakov, D. W. deQuilettes, A. Sadhanala, W. Li, L. Wang, D. S. Ginger, R. H. Friend, H. J. Snaith, *Nat. Commun.* **2015**, *6*.
[22]   G. Li, T. Zhang, Y. Zhao, *J. Mater. Chem. A* **2015**, *3*, 19674.

[23]   P.-W. Liang, C.-Y. Liao, C.-C. Chueh, F. Zuo, S. T. Williams, X.-K. Xin, J. Lin, A. K. Y. Jen, *Adv. Mater.* **2014**, *26*, 3748.
[24]   C. Zuo, L. Ding, *Nanoscale* **2014**, *6*, 9935.
[25]   W. Zhang, M. Saliba, D. T. Moore, S. K. Pathak, M. T. Hörantner, T. Stergiopoulos, S. D. Stranks, G. E. Eperon, J. A. Alexander-Webber, A. Abate, A. Sadhanala, S. Yao, Y. Chen, R. H. Friend, L. A. Estroff, U. Wiesner, H. J. Snaith, *Nat. Commun.* **2015**, *6*, 6142.
[26]   Y. Zhao, K. Zhu, *J. Phys. Chem. C* **2014**, *118*, 9412.
[27]   J. Berry, T. Buonassisi, D. A. Egger, G. Hodes, L. Kronik, Y.-L. Loo, I. Lubomirsky, S. R. Marder, Y. Mastai, J. S. Miller, D. B. Mitzi, Y. Paz, A. M. Rappe, I. Riess, B. Rybtchinski, O. Stafsudd, V. Stevanovic, M. F. Toney, D. Zitoun, A. Kahn, D. Ginley, D. Cahen, *Adv. Mater.* **2015**, *27*, 5102.
[28]   T. Jesper Jacobsson, J.-P. Correa-Baena, M. Pazoki, M. Saliba, K. Schenk, M. Gratzel, A. Hagfeldt, *Energy Environ. Sci.* **2016**, *9*, 1706.
[29]   D. Solis-Ibarra, I. C. Smith, H. I. Karunadasa, *Chem. Sci.* **2015**, *6*, 4054.
[30]   W. Zhu, C. Bao, F. Li, T. Yu, H. Gao, Y. Yi, J. Yang, G. Fu, X. Zhou, Z. Zou, *Nano Energy* **2016**, *19*, 17.
[31]   Z. Zhou, Z. Wang, Y. Zhou, S. Pang, D. Wang, H. Xu, Z. Liu, N. P. Padture, G. Cui, *Angew. Chem. Int. Ed.* **2015**, *54*, 9705.
[32]   Y. Zhou, M. Yang, S. Pang, K. Zhu, N. P. Padture, *J. Am. Chem. Soc.* **2016**, *138*, 5535.
[33]   J. Xiao, Y. Yang, X. Xu, J. Shi, L. Zhu, S. Lv, H. Wu, Y. Luo, D. Li, Q. Meng, *J. Mater. Chem. A* **2015**, *3*, 5289.
[34]   F. Huang, Y. Dkhissi, W. Huang, M. Xiao, I. Benesperi, S. Rubanov, Y. Zhu, X. Lin, L. Jiang, Y. Zhou, A. Gray-Weale, J. Etheridge, C. R. McNeill, R. A. Caruso, U. Bach, L. Spiccia, Y.-B. Cheng, *Nano Energy* **2014**, *10*, 10.
[35]   J. Kim, J. S. Yun, X. Wen, A. M. Soufiani, C. F. J. Lau, B. Wilkinson, J. Seidel, M. A. Green, S. Huang, A. W. Y. Ho-Baillie, *J. Phys. Chem. C* **2016**, *120*, 11262.
[36]   B. Xia, Z. Wu, H. Dong, J. Xi, W. Wu, T. Lei, K. Xi, F. Yuan, B. Jiao, L. Xiao, Q. Gong, X. Hou, *J. Mater. Chem. A* **2016**, *4*, 6295.
[37]   K. Hwang, Y.-S. Jung, Y.-J. Heo, F. H. Scholes, S. E. Watkins, J. Subbiah, D. J. Jones, D.-Y. Kim, D. Vak, *Adv. Mater.* **2015**, *27*, 1241.
[38]   H. Miyamae, Y. Numahata, M. Nagata, *Chem. Lett.* **1980**, *6*, 663.
[39]   W. Li, J. Fan, J. Li, Y. Mai, L. Wang, *J. Am. Chem. Soc.* **2015**, *137*, 10399.
[40]   N. Ahn, D.-Y. Son, I.-H. Jang, S. M. Kang, M. Choi, N.-G. Park, *J. Am. Chem. Soc.* **2015**, *137*, 8696.
[41]   S. Bae, S. J. Han, T. J. Shin, W. H. Jo, *J. Mater. Chem. A* **2015**, *3*, 23964.
[42]   Y. Jo, K. S. Oh, M. Kim, K.-H. Kim, H. Lee, C.-W. Lee, D. S. Kim, *Adv. Mater. Interfaces* **2016**, DOI: 10.1002/admi.201500768.
[43]   Y. Wu, A. Islam, X. Yang, C. Qin, J. Liu, K. Zhang, W. Peng, L. Han, *Energy Environ. Sci.* **2014**, *7*, 2934.
[44]   J. S. Manser, M. I. Saidaminov, J. A. Christians, O. M. Bakr, P. V. Kamat, *Acc. Chem. Res.* **2016**, *49*, 330.
[45]   J. Cao, X. Jing, J. Yan, C. Hu, R. Chen, J. Yin, J. Li, N. Zheng, *J. Am. Chem. Soc.* **2016**, *138*, 9919.
[46]   N. Arora, M. I. Dar, M. Hezam, W. Tress, G. Jacopin, T. Moehl, P. Gao, A. S. Aldwayyan, B. Deveaud, M. Grätzel, M. K. Nazeeruddin, *Adv. Funct. Mater.* **2016**, *26*, 2846.
[47]   Y. Zhou, O. S. Game, S. Pang, N. P. Padture, *J. Phys. Chem. Lett.* **2015**, *6*, 4827.
[48]   D. P. McMeekin, G. Sadoughi, W. Rehman, G. E. Eperon, M. Saliba, M. T. Hörantner, A. Haghighirad, N. Sakai, L. Korte, B. Rech, M. B. Johnston, L. M. Herz, H. J. Snaith, *Science* **2016**, *351*, 151.
[49]   M. Saliba, T. Matsui, J.-Y. Seo, K. Domanski, J.-P. Correa-Baena, M. K. Nazeeruddin, S. M. Zakeeruddin, W. Tress, A. Abate, A. Hagfeldt, M. Gratzel, *Energy Environ. Sci.* **2016**, *9*, 1989.
[50]   N. J. Jeon, J. H. Noh, W. S. Yang, Y. C. Kim, S. Ryu, J. Seo, S. I. Seok, *Nature* **2015**, *517*, 476.
[51]   Q. Wang, Y. Shao, Q. Dong, Z. Xiao, Y. Yuan, J. Huang, *Energy Environ. Sci.* **2014**, *7*, 2359.
[52]   C. Roldan-Carmona, P. Gratia, I. Zimmermann, G. Grancini, P. Gao, M. Graetzel, M. K. Nazeeruddin, *Energy Environ. Sci.* **2015**, *8*, 3550.
[53]   S. Pang, H. Hu, J. Zhang, S. Lv, Y. Yu, F. Wei, T. Qin, H. Xu, Z. Liu, G. Cui, *Chem. Mater.* **2014**, *26*, 1485.
[54]   K. Miyano, M. Yanagida, N. Tripathi, Y. Shirai, *J. Phys. Chem. Lett.* **2016**, *7*, 2240.
[55]   L. Meng, J. You, T.-F. Guo, Y. Yang, *Acc. Chem. Res.* **2016**, *49*, 155.
[56]   Q. Wang, Q. Dong, T. Li, A. Gruverman, J. Huang, *Adv. Mater.* **2016**, DOI: 10.1002/adma.201600969.
[57]   C. Kuang, G. Tang, T. Jiu, H. Yang, H. Liu, B. Li, W. Luo, X. Li, W. Zhang, F. Lu, J. Fang, Y. Li, *Nano Lett.* **2015**, *15*, 2756.
[58]   B. Conings, J. Drijkoningen, N. Gauquelin, A. Babayigit, J. D'Haen, L. D'Olieslaeger, A. Ethirajan, J. Verbeeck, J. Manca, E. Mosconi, F. D. Angelis, H.-G. Boyen, *Adv. Energy Mater.* **2015**, *5*, 201500477.
[59]   B. Yang, O. Dyck, J. Poplawsky, J. Keum, A. Puretzky, S. Das, I. Ivanov, C. Rouleau, G. Duscher, D. Geohegan, K. Xiao, *J. Am. Chem. Soc.* **2015**, *137*, 9210.
[60]   A. Pisoni, J. Jacimovic, B. Náfrádi, P. Szirmai, M. Spina, R. Gaál, K. Holczer, E. Tutis, L. Forró, E. Horváth, *arXiv:1604.05637v1* **2016**.
[61]   K. Wojciechowski, T. Leijtens, S. Siprova, C. Schlueter, M. T. Hörantner, J. T.-W. Wang, C.-Z. Li, A. K. Y. Jen, T.-L. Lee, H. J. Snaith, *J. Phys. Chem. Lett.* **2015**, *6*, 2399.
[62]   C. Tao, S. Neutzner, L. Colella, S. Marras, A. R. Srimath Kandada, M. Gandini, M. D. Bastiani, G. Pace, L. Manna, M. Caironi, C. Bertarelli, A. Petrozza, *Energy Environ. Sci.* **2015**, *8*, 2365.
[63]   K. Wojciechowski, S. D. Stranks, A. Abate, G. Sadoughi, A. Sadhanala, N. Kopidakis, G. Rumbles, C.-Z. Li, R. H. Friend, A. K. Y. Jen, H. J. Snaith, *ACS Nano* **2014**, *8*, 12701.

[64]   Y. Li, Y. Zhao, Q. Chen, Y. Yang, Y. Liu, Z. Hong, Z. Liu, Y.-T. Hsieh, L. Meng, Y. Li, Y. Yang, *J. Am. Chem. Soc.* **2015**, *137*, 15540.

[65]   J. T.-W. Wang, Z. Wang, S. K. Pathak, W. Zhang, D. deQuilettes, F. Wisnivesky, J. Huang, P. Nayak, J. Patel, h. yusof, Y. Vaynzof, R. Zhu, I. Ramirez, J. Zhang, C. Ducati, C. Grovenor, M. Johnston, D. S. Ginger, R. Nicholas, H. Snaith, *Energy Environ. Sci.* **2016**, DOI: 10.1039/C6EE01969B.